Massive and localized export of selected marine snow types at eddy edges in the South Atlantic Ocean

Alexandre Accardo[1], Rémi Laxenaire[4,5,6], Alberto Baudena[1], Sabrina Speich[3,4], Rainer Kiko[2], Lars Stemmann[1]

[1]Sorbonne Université, CNRS, Laboratoire d'Océanographie de Villefranche, UMR 7093 LOV, Villefranche-sur-Mer, France
[2]GEOMAR Helmholtz Center for Ocean Research Kiel, Germany
[3]Ecole Normale Supérieure, PSL Research University, France
[4]UMR 8539 Laboratoire de météorologie dynamique (LMD), France
[5]UMR 8105 Laboratoire de l'Atmosphère et des Cyclones, Saint-Denis de La Réunion, France
[6]Center for Ocean-Atmospheric Prediction Studies, Florida State University, Tallahassee, FL, United States

Correspondence to: Alexandre Accardo (alexandre.accardo@imev-mer.fr)

Abstract

The open ocean plays a critical role in mitigating climate change by sequestering carbon dioxide (CO_2) from the atmosphere for long periods of time. This carbon storage occurs over decades to millennia and relies on the physical pump that transports cold, dense, and DIC-rich waters to the deep ocean, as part of the ocean's overturning circulation, and the biological carbon pump (BCP). The BCP encompasses a wide range of processes, from the fixation of atmospheric CO_2 by phytoplankton activity to carbon sequestration in the deep ocean. Atmospheric CO_2 concentrations would be about 200 ppm higher than in a world without biology, and the global climate would be much warmer by default. This study highlights the idea that BCP efficiency is enhanced by the ocean dynamics at mesoscale and submesoscale. In fact, our results suggest that frontal regions, such as those between mesoscale eddies, could lead to an important accumulation and transport of particulate organic matter (POM) from the mixed layer depth (MLD) down to depths of about 600 meters. To reach these conclusions, a multifaceted approach was applied. It included in-situ measurements and marine snow images from a BGC Argo float equipped with an Underwater Vision Profiler (UVP6), satellite altimetry data, and Lagrangian physics diagnostics. We focused our study on three intense features in marine snow distribution observed during the 17-month long float mission in the Cape Basin, southwest of Africa. These features were located in the frontal region between mesoscale eddies. Our study suggests that a particle injection pump induced by a frontogenesis-driven mechanism has the potential to enhance the effectiveness of the biological pump by increasing the depth at which carbon is injected into the water column. This work also emphasizes the importance of establishing repeated sampling campaigns targeting the interface zones between eddies. This could improve our understanding of the mechanisms involved in the deep accumulation of marine snow observed at eddy interfaces.

1 Introduction

The open ocean plays a critical role in mitigating climate change by storing carbon dioxide (CO_2) away from the atmosphere for long periods of time (Boyd et al., 2019). This carbon storage occurs over decades to thousands of years and relies on two well-established mechanisms that create a gradient of dissolved inorganic carbon (DIC) between the surface and deep regions of the ocean and enhances DIC concentrations at depth. These mechanisms are known as the biological pump and the solubility pump (or physical pump). The solubility pump transports cold, dense, and DIC-rich waters to the deep ocean, as part of the ocean's overturning circulation, primarily in high-latitude regions. The biological carbon pump (BCP), on the other hand, involves the export of particulate organic carbon (POC) from surface waters below the euphotic depth, and operates worldwide. The BCP encompasses a wide range of processes, from the fixation of atmospheric CO_2 by phytoplankton activity, to carbon sequestration into the deep ocean (Le Moigne, 2019). The BCP contributes also to approximately 90% of the dissolved inorganic carbon (DIC) gradient between surface and deep ocean (Boyd et al., 2019). Without the BCP atmospheric concentrations of the greenhouse gas CO_2 would be approximately 200 ppm higher than in a world without biology (Maier-Reimer et al. 1996) and the global climate would be much warmer by default.

A key component of the BCP is the biological gravitational pump (BGP). The BGP is the process by which large and/or dense aggregates of particulate organic carbon (POC), typically produced by phytoplankton activity, sink under gravity. POC, also called marine snow (for particles >500μm), can consist of aggregated phytoplankton cells such as diatoms, different types of aggregates resulting from coagulation processes (Le Moigne, 2019), and zooplankton faecal pellets (Turner, 2015). This mechanism is estimated to export about 6 Pg of carbon per year below the mixed layer depth (MLD; Boyd et al., 2019). The rate at which surface aggregates sinks to the deep ocean depends on their individual sinking rates, which are influenced by their combined morphological (size, porosity, etc.) and chemical properties (ratio of organic versus mineral, mineral type, etc.) (Stemmann et al., 2004; Cael et al., 2021). Sinking rates of different types of marine snow types have been estimated to range from 10 to 100 m d-1 from laboratory experiments (Shanks and Trent, 1980; Azetsu-Scott and Johnson, 1992) and, in a few cases, from in situ imaging time series (Alldredge and Gotschalk, 1988; Stemmann et al., 2002; Trudnowska et al., 2022). In situ imaging of marine snow allows us to observe the change in size and morphology of aggregates as they progress through the ocean interior. This can improve our understanding of particle dynamics and, hopefully, their sinking rates, which affect the BGP.

Another important component of the BCP that can occur concurrently with the BGP, are the particle injection pumps (PIPs). These consist of the export of carbon mediated by plankton migrations or physical vertical movement and can also play a significant role in the ocean's capacity to store carbon. PIPs encompass a variety of mechanisms, temporal-spatial scales, and geographical extent, and can affect all types of particles, from those suspended in the water column to sinking particles. They typically transport particles below the euphotic zone. Depending on the specific injection mechanism, PIPs can reach depths greater than 1000 m (Boyd et al. 2019). Due to their dynamic nature, which includes physical transport or the patchy

62   distribution of animals, the interaction between the vertical and horizontal components of PIPs, as well as their temporal scales,
63   can vary significantly (Boyd et al., 2019). The physical processes that make up the PIPs include subduction resulting from the
64   mixed-layer shallowing (referred to as the mixed-layer pump), subduction caused by the large-scale ocean circulation over
65   distances of 100-1000 km (referred to as the large-scale subduction pump), and subduction mediated by mesoscale (10-100
66   km, few weeks to several months) to submesoscale (1-10 km, hours to days) ocean dynamics.

67   In particular, the influence of mesoscale eddies on particle production, aggregation and export (McGillicuddy, 2016) is a very
68   active area of research because these structures are ubiquitous in the global ocean and are the largest source of ocean variability
69   (Stammer, 1997; Wunsch, 1999). They also play an important role in the vertical distribution of water mass properties as they
70   are associated with upwelling and downwelling. Upwelling results in the transport of nutrients to the surface mixed layer which
71   normally enhances productivity. Downwelling results in the physical transport of dissolved, and particulate (both sinking and
72   suspended) carbon to depth. Understanding the mechanisms associated with physical-biological biogeochemical interaction is
73   challenging due to the transient nature of the underlying processes. Therefore, it is essential to employ multidisciplinary
74   approaches, including in situ observations, to elucidate these intricate phenomena (McGillicuddy, 2016).

75   The aim of the present work is to understand how frontogenesis mechanisms induced by mesoscale activity coupled with the
76   gravitational carbon pump can lead to the rapid accumulation of diverse particulate matter ranging from 5 μm to 16 mm in
77   size at depths exceeding 600 meters. This work is based on the deployment of a new prototype of BGC Argo float (part of the
78   Argo international program: https://argo.ucsd.edu) equipped with an Underwater Vision Profiler 6 (UVP6; Picheral et al.,
79   2022) and several physical-biogeochemical sensors in the Southeast Atlantic Ocean. The float was deployed in the Cape Basin,
80   a region southwest of Africa, known for its intense eddy activity, which is mainly controlled by a complex interaction between
81   the Benguela Upwelling, the Agulhas Current System and the South Atlantic Current (Richardson et al., 2003; Boebel et al.,
82   2003). The float was recovered after one year of operation and the collected images were analyzed and classified into plankton
83   categories and morphological types of marine snow (Trudnowska et al., 2022). Hydrological and particle data collected by the
84   float were then combined with satellite altimetry to identify frontal structures and mesoscale eddies (Chaigneau et al., 2009;
85   Laxenaire et al., 2018; 2019; 2020).

86   **2 Material and Methods**

87   **1.1 Observing strategy**

88   During the SO283 cruise, a BGC Argo float (WMO: 6903095) was deployed on April 14, 2021, in a cyclonic eddy in the
89   southeastern region of the Atlantic Ocean, near the Benguela upwelling system at 33.0978°S and 13.8673°E (Fig. 1). The float
90   remained within the eddy for about 5 months (Baudena et al. 2023, preprint), until the eddy disappeared from satellite altimetry
91   maps probably because of subduction in the ocean interior (Ioannou et al., 2022). It then sampled different mesoscale features

92 within the region, and after a sampling period of about 1.5 years, it was retrieved by the S.A. Agulhas II on September 19,

93 2022. During its deployment, the float completed a total of 183 profiles, the majority of which were acquired from the surface

94 down to 600- or 1000-meter depth.

1.2 Environmental data

96 The float was equipped with several sensors to quantify seawater properties along the water column. The float was

97 instrumented with pressure (DRUCK_2900PSIA, SN: 11587115), temperature and salinity sensors (SBE41CP_V7.2.5, SN:

98 13100) to measure the hydrological water properties. The biogeochemical properties were measured with oxygen

99 (AANDERAA_OPTODE_4330, SN: 3489), fluorescence and backscattering (700 nm) sensors (ECO_FLBB_2K, SN: 6310).

100 All the BGC Argo data that were used in this work, are made freely available by the International Argo Program

101 (https://fleetmonitoring.euro-argo.eu/float/6903095). Before analysis, some derived variables were calculated based on a

102 Python implementation of the Gibbs SeaWater (GSW) Oceanographic Toolbox of TEOS-10 (http://www.teos-10.org/). Firstly,

103 Absolute Salinity (SA) was computed from Practical Salinity (PSAL) and pressure (dbar) measurements and Conservative

104 Temperature (CT, °C) was computed from in-situ Temperature (T, °C). These two variables were then used to calculate the

105 Potential Density (kg.m^{-3}) with a reference pressure of 0 dbar (Roquet et al., 2015). Regarding the oxygen parameter, the

106 Apparent Oxygen Utilization (AOU, μmol.kg^{-3}) was computed as the difference between the oxygen concentration expected

107 at equilibrium with air and the in-situ oxygen concentrations. The expected oxygen concentration was computed from

108 solubility coefficients derived from the data of Benson and Krause (1984), as fitted by Garcia and Gordon (1992). Finally, the

109 mixed layer depth (MLD), which is the upper part of the water column where salinity, temperature, and density remain

110 vertically constant, was detected following De Boyer Montégut (2004). A reference value for density was taken at 5 dbar and

111 the water column was considered to be mixed until the depth at which density deviates from this reference by more than 0.03

112 kg.m^{-3}

1.2 Living and non-living particle data

1.1.1 Small phytoplanktonic and bulk particles

115 To estimate chlorophyll-a concentrations emitted by phytoplanktonic cells, the float was equipped with a fluorescence sensor

116 (ECO_FLBB_2K, SN: 6310). The backscattering (700 nm) sensor (ECO_FLBB_2K, SN: 6310) was used to quantify the

117 amount of all particles (including detritus and phytoplankton). The backscattering coefficient signal (*bbp*) was decomposed to

118 extract the signal of small labile and refractory particles (*bbsr*) from the raw signal which also contained spikes triggered by

119 rare large aggregates passing in the flow field. This was done by applying the method proposed by Briggs et al., 2020 (see

120 supplementary materials). The *bbsr* signal represented the distribution of particles between 5 to 20 μm.

1.2.2 Underwater Vision Profiler 6 (UVP6-LP)

The float was also equipped with an in-situ camera, the Underwater Vision Profiler 6 Low-Power (UVP6-LP, SN: 000101) specifically designed to be deployed on autonomous platforms. The UVP6 detects and measures the size (from 0.102 to 16.40 mm in Equivalent Spherical Diameter, ESD) of zooplankton and various biogenic matter such as POC (Particulate Organic Carbon), marine snow and fecal pellets. Thanks to the float recovery, images of objects >500 μm could be retrieved as well and therefore, taxonomic identification of macrozooplankton and large particle classification could be conducted. A more detailed description of the UVP6-LP can be found in Picheral et al., 2022.

1.2.3 A broad size classification of particles (MiP and MaP)

To conduct a community analysis of marine snow and examine their spatio-temporal distribution, we applied a rough size classification on raw size- spectra data (>100 μm) provided by the UVP6 (without any plankton identification). In this case the assumption was made that zooplankton represents only a small fraction of objects sampled by the UVP6 (14.5% of images) compared to particles (85.5%). Hence, we consider its contribution as neglectable for this purpose. Then, all size-spectra were divided into two sub-classes: MiP (Micrometric Particles) and MaP (Macroscopic Particles). MiP concentrations were obtained by integrating the concentrations overall size classes between 0.1- and 0.5-mm. MaP concentrations were computed exactly in the same way but considering all size classes between 0.5- and 16-mm. The 0.5 mm threshold was used as detrital aggregates > 0.5 mm are considered marine snow (i.e., aggregates, Alldredge and Gotschalk, 1988).

1.2.4 Unsupervised morphological classification of marine snow

To better characterize the marine snow dynamics, an unsupervised classification method was used, following the previous study on particle dynamics in the Arctic Ocean (Trudnowska et al., 2021). This provides information on particle size, shape, gray level, and heterogeneity. This method allows one to classify rapidly and efficiently particle images in objective categories. In summary, firstly, zooplankton and detrital particle images were separated, by manual validation and treated independently. After this separation, a PCA was performed on morphological traits of the detrital particle images. Those specific traits represented their size (e.g., area, perimeter), shade intensity (e.g., mean/median gray level), shape (e.g., symmetry, elongation), and structure (i.e., homogeneity or heterogeneity, mostly based on the variability in gray level). To obtain a normal distribution for each variable, extreme values (in that they were below or above the first and 95th percentile) were removed and each variable was transformed by the Yeo-Johnson transformation (Yeo, 2000). This PCA led to the creation of a morphospace in which each particle image can be located based on their morphological features. Then, a K-means clustering was performed on this new morphospace using the first five principal components. The number of clusters, "k", was set to four. This specific number, after several simulations, was chosen because it conducted the best partitioning with four clearly different groups of particle morphology.

151 Finally, the concentration (nb.m^{-3}) of each morphotype was computed by multiplying the number of particles found in each

152 cluster and depth bin by the volume sampled by the UVP6. To study their spatio-temporal distributions, group concentrations

153 were interpolated according to depth and time with a resolution of 5 meters and one day respectively.

154 Since some groups in the morphospace partially overlap (Fig. 5B), potentially affecting the quality of the classification, a

155 further selection process was implemented. This involved calculating the Euclidean distance between individual particle

156 images and their respective cluster centers. Subsequently, for each group, the first quartile distance was computed, and only

157 individuals with a distance smaller than the first quartile were included in the selection. These 'new' members (called

158 'exclusive members') were then used as indicators to see potential differences in the distribution pattern of each morphotype.

159

1.2.5 Selection of profiles corresponding to deep massive exports

161 To characterize in an objective way significant changes in the deep marine snow spatio-temporal distribution, the Sequential

162 T-test Analysis of Regime Shifts (STARS) method was used (Rodionov, 2004). This method, based on the Student's t-test2,

163 analyses a dataset in a sequential manner. It compares each new observation with all the entries in the current 'regime' or group.

164 If an entry significantly deviates from the average of that regime, it is marked as a potential 'shift point'. The algorithm then

165 tests whether this detected shift is persistent over time. To characterize significant changes in the water column, marine snow

166 concentrations were integrated, for each UVP6 profile, between 150 and 600 meters. Then, profiles detected in each significant

167 'shift' were selected and considered as belonging to (or 'inside') those features in marine snow distribution (see Fig. S1).

168 Afterward, to compare the aggregates distribution outside and inside each feature, profiles one month before and one month

169 after each feature were selected and merged, providing the mean of particle concentrations 'outside' each feature. The same

170 protocol was applied to study the morphotype proportions according to depth. The latter were computed in four depth layers,

171 between 0-100, 100-300, 300-600 and 600-1000 meters to see the evolution of the morphotypes relative abundance overall the

172 water column.

173

1.3 Satellite data and the TOEddies algorithm

175 To identify mesoscale eddies, we implemented the TOEddies algorithm (The Ocean Eddy Detection and Tracking Algorithm,

176 Laxenaire et al., 2018). TOEddies is based on the identification of mesoscale eddies as closed contours of Sea Surface Height

177 (SSH) surrounding an extremum. This relies on the principle that in a geostrophic balance, SSH isolines align with current

178 streamlines. As a result, a maximum (minimum) SSH that is surrounded by a closed circulation is classified as an anticyclonic

179 (cyclonic) eddy. To track the eddies over time, the algorithm takes advantage of the fact that daily eddy displacements are

180 small compared to their dimensions, resulting in overlapping areas between successive days. This methodology allows the

181 derivation of trajectories and the detection of events where eddies merge or split, providing a mechanism for tracing the origin

182 of sampled water masses—a critical component for the objectives of this study.

183   For the purposes of this study, the TOEddies algorithm was applied to the Absolute Dynamic Topography (ADT, a proxy for

184   SSH) and its associated with geostrophic currents. These ¼ gridded daily maps are produced by Ssalto/Duacs and distributed

185   by the Copernicus Marine Environment Monitoring Service (http://marine.copernicus.eu/) in the version released in April 2018

186   (DT18; Pujol et al., 2016; Ballarotta et al., 2019). Each identified eddy was characterized by two radii associated to the two

187   eddy boundaries defined in TOEddies: the outermost contour (Rout), and the contour with the maximum averaged geostrophic

188   velocities (Rmax and associated velocity Vmax).

189   Eddies identified by the algorithm were collocated with float profiles (Chaigneau et al., 2011; Laxenaire et al., 2019; 2020).

190   This allows us to categorize the profiles according to whether they sampled a cyclone, an anticyclone, a region outside of the

191   influence of mesoscale eddies, or an area at the interface of two eddies. The application of TOEddies to ADT maps, coupled

192   with the collocation of detected eddies with Argo profiles, has proven to be a successful combination for exploring eddy

193   dynamics in the southeast Atlantic (Laxenaire et al., 2019,2020; Ioannou et al.,2022; Baudena et al., 2023).

194   **1.4 Lagrangian diagnostics**

195   Several Lagrangian diagnostics have been computed at the location of each profile using satellite-derived currents and

196   environmental variables. First, for each station (i.e., profile location), a region was defined as representative of the water parcel

197   sampled by the float. In this study, this region was a circular neighborhood with a radius r of 0.1° around each profile location.

198   This distance allowed us to smooth the satellite uncertainties and has been used in previous studies (Chambault et al., 2019;

199   Baudena et al., 2021; Ser-Giacomi et al., 2021; Fabri-Ruiz et al., 2023). This circular shape was then filled with virtual particles

200   (nearly 300) separated by 0.01°. Then, for each virtual particle, a given Lagrangian diagnostic was computed (detailed below).

201   This resulted in about 300 values for each sampling station. These have been averaged, leading to a value of a given Lagrangian

202   diagnostic for each profile. The velocity field we used have been derived from both altimetry and delayed-time model

203   assimilation data and includes both the geostrophic and the Ekman components (Copernicus CMEMS product MULTIOBS

204   GLO PHY REP 015 004-TDS). It has been used backward in time to advect each virtual particle (within the representative

205   water parcel) from the profile day until an advective time (τ). Different τ values were used, ranging from 5 to 45 days. Hence,

206   for each profile, each diagnostic has been calculated using different advective times. The first diagnostic we implemented was

207   the Finite-Time Lyapunov Exponents (FTLE, days-1; Shadden et al., 2005). This metric is useful for identifying fronts. A front

208   is defined as a physical barrier that separates two adjacent water masses that have been widely separated in the preceding days

209   and are likely to have different hydrographic properties. FTLEs were computed as in Shadden et al., (2005), with an initial

210   separation of 0.1°. We implemented as a second diagnostic the Lagrangian chlorophyll-a ($mg.m^{-3}$), which is the mean

211   chlorophyll content calculated along the backward virtual particle trajectory. This diagnostic determines whether the seawater

212   parcel sampled at a profile location was rich in chlorophyll in the preceding days. For the chlorophyll, we used the delayed-

213   time satellite product "OCEANCOLOUR GLO BGC L4 MY 009 104-TDS" provided by CMEMS Copernicus website (0.25°

214   resolution, provided daily).

215

2 Results

2.1 Circulation and water mass spatio-temporal distribution

The study area exhibits significant environmental variability, in terms of water masses and their spatio-temporal variability in relation to intense mesoscale activity (Fig. 2). Visual inspection of the TOEddies algorithm results, coupled with analysis of hydrological data provided important information about the history and origin of the water masses sampled by the float. In the following, we separate the life history of the float trajectory in different periods. During April to October 2021 (fall and winter), the float was trapped within a cyclonic eddy shed from the southern Benguela upwelling front (Baudena et al., 2023, preprint). During this period, temperature, salinity, and density were relatively stable. Figure 2 shows that the MLD varied between near-surface depths and 200 m. Analysis of the AOU time series shows predominantly weak positive or even negative values only above the MLD (Fig. 2.F). Regarding the FTLE time series, values remained low compared to the entire time series (less than 0.25 days^{-1}) except around August 2021 when the targeted eddy merged with another Benguela Upwelling cyclone (0.45 days^{-1}). Overall, the float remained near the center of the cyclonic eddy, which explains the low FTLE values. After the merging, the float continued to move within the new cyclonic structure. This cyclonic eddy merged again (in early October 2021) with an Agulhas cyclone that formed along the Agulhas Bank, the southern shelf-edge of Africa (Penven et al., 2001; Lutjeharms et al., 2003). This type of cyclone originates from the southern African continental slope from barotropic instabilities and enters the ocean interior at the northern edge of the Agulhas Current Retroflection (Duncombe Rae, 1991) with very different hydrographic characteristics compared with the Benguela upwelling cyclones.

After exiting the cyclone, the float remained within its periphery. In mid-October, the float was at the interface between the cyclone and an anticyclonic eddy. Then, the float moved southward until May 2022. The water column was more stratified and characterized by a shallower MLD (typical for spring and summer). During this period, two phases of the life history of the float can be identified. During the first phase, warmer and saltier waters were observed between 200 and 800 m depth. These waters clearly originate from Agulhas Current water masses, very likely originating from an injection in the region of the Agulhas rings generated at the Agulhas Current Retroflection (Laxenaire et al., 2018). The second phase is characterized by colder and fresher water masses. Indeed, between January and March 2022, the float crossed the Subantarctic front and continued to move southward along the edge of an Agulhas ring, a relatively old Agulhas cyclone, as well as a Subantarctic Front cyclone. Finally, in April 2022, the float passed next to another Subantarctic Front cyclone, which could explain the colder and less salty water masses during this period. Moreover, specific patterns in the AOU and the density time series are also observed during the transition between these two phases. Indeed, the AOU time series shows smaller values (close to 0 µmol.m^{-3}) at depths between 200 and 1000 m. The latter are also associated with important horizontal isopycnal variations (steep slopes), reaching depths close to 900 m and coinciding with high FTLE values (above 0.45 days^{-1}).

The final period spans May to September 2022 and is marked by three high-intensity mesoscale features that influence the water column down to about 800 to 1000 m depth. These features are characterized by a deeper MLD and the presence of

248   much warmer and saltier water masses all over the water column. The AOU time series shows a strong signal during this
249   period, with negative values observed at depths around 800 m. This period was also characterized by intense FTLE values
250   throughout. The TOEddies analysis showed that the float profiled different cyclones and anticyclones during this period.

251   In summary, during its deployment, the float sampled water masses with significantly different hydrological characteristics
252   and from multiple geographical zones. At this stage, one of the main results to keep in mind is that the float sampled interface
253   zones between anticyclonic and cyclonic structure. Overall, these observations highlight the dynamic nature of the study area,
254   characterized by contrasting water mass properties and their temporal variations throughout the year.

2.2 Spatio-temporal distribution of marine snow during the survey

256   From April to October 2021 (Fall and Winter), surface chlorophyll-a concentrations and the *bbsr* coefficient remained
257   relatively low (Fig. 2.E.F). Afterwards, a significant change occurred between the end of October 2021 and May 2022 (Spring
258   and Summer). This period coincided with the seasonal production of phytoplankton, as evident in the chlorophyll-a
259   concentration time series. There was also an observable increase in the concentration of small, labile, and refractory particles
260   in the surface, as reflected by the *bbsr* coefficient (Fig. 2.E). Moving forward to the period between May and September 2022,
261   there was a noticeable decline in chlorophyll-a concentration. Consequently, weaker concentrations were observed at the
262   surface, and the *bbsr* coefficient was also reduced. In general, the spatio-temporal dynamics of MiP and MaP exhibit notable
263   differences (Fig. 3). MiPs were generally more abundant than MaPs, ranging between 1.5- and 7.5 part.L^{-1}, while MaP
264   concentrations ranged from 0 to 1.6 part.L^{-1} (Fig. 3). Both types of particles displayed higher mean concentrations above the
265   MLD than below. MiP were consistently present throughout the float deployment, with a slightly higher abundance observed
266   between October 2021 and May 2022. Conversely, the distribution pattern of MaPs differed. Their concentration was relatively
267   low from the beginning of the time series until October 2021. Subsequently, their surface abundance significantly increased
268   during the phytoplankton production period between the end of October 2021 and May 2022. Overall, these observations
269   highlight the distinct spatio-temporal dynamics of MiP and MaP. A key result in the marine snow spatial distribution is that
270   three different "columns" of increased particle concentration (in particular MaPs) were observed between the surface down to
271   600 meters. These features lasted for approximately a month. The first one took place between October 8 and 23, 2021, the
272   second one occurred from November 25 to December 22, 2021, and finally, the last one spanned approximately between March
273   3 and April 28, 2022.

2.3 Spatio-temporal distribution of MaP morphological groups during the survey

275   The unsupervised clustering method led to the identification of four morphotypes distinguished by their size, circularity,
276   brightness, and homogeneity (Fig. 5.A.B). The first morphotype was characterized by small, dark, and predominantly circular
277   particles. The second morphotype comprised elongated objects with varying degrees of brightness. The third morphotype
278   consisted of bright, fluffy, and diverse marine snow particles. The fourth morphotype encompassed larger marine snow

279 particles, often with the form of aggregated structures with some heterogeneity. All the identified morphotypes were
280 predominantly found in the surface layer. Specifically, the elongated particles (Fig. 6.B) exhibited a distinct concentration
281 increase from late September 2021, maintaining a stable abundance until early May 2022. Before and after this period, their
282 presence was considerably smaller. Additionally, these elongated particles displayed a strong positive correlation with
283 chlorophyll-a concentration in the surface layer (0-100m), as evidenced by a significant Spearman correlation coefficient of
284 0.65 (p-value = $9.3.10^{-22}$, Fig. S2). In contrast, the other three morphotypes (small, bright, and aggregates, Fig. 6.A.C.D)
285 exhibited different dynamics. They were present in all three MaP features described above, whereas the elongated particles
286 did not appear to be extensively involved. The dense aggregates morphotype (purple in Fig. 5.C) is the most abundant during
287 these three features (Fig. 6.A-C).

2.4 Vertical distribution of particle community composition inside and outside massive export features

289 Here we analyze the distribution of the four morphotypes in the water column during the three export features (Fig. 5.D).
290 Indeed, a shift is observed in their relative proportion between the surface and the layers below. Specifically, the abundance
291 of small particles (salmon pink in Fig. 5.D) and dense aggregates (purple) increases, while the proportion of elongated and
292 bright morphotypes decreases. For example, in column 3, the proportion of small morphotypes incremented from 12% to 23%
293 and from 25% to 47% in dense aggregates. Furthermore, the distribution of morphotypes within each export feature did not
294 change considerably, except perhaps in the case of column 2.

2.5 The eddy dynamic context

296 The first and the second export feature occurred at the boundary between a cyclonic and an anticyclonic eddy (Fig. 7). This
297 region was therefore characterized by very intense submesoscale frontal dynamics. During the second feature (Fig. 8), the
298 position of the cyclone did not change significantly. The float entered the cyclone but remained close to its R_{Vmax} boundary
299 and thus within the submesoscale frontal region of the cyclone edge. Indeed, the eddy frontal regions extend over an area of
300 10-20 km across the region of eddy maximum azimuthal velocity (i.e., across R_{Vmax}) as shown in Barabinot et al., (2023). This
301 second feature ended when the float was expelled from the cyclone and began to be advected southward, leaving the frontal
302 region. The third export occurred when the float was advected around the southern edge of a large anticyclone (Fig. 9), again
303 a submesoscale frontal region.

2.6 Impact of the three features on the upper 600m water column

305 Figure 4 clearly illustrates the high abundance of particulate carbon associated with the three export columns, with their
306 influence extending down to 600 m depth. The abundance increased by a factor of 2-3 (with a factor of more than 7 during the
307 first feature) compared to periods when the Argo float was moving 'outside' these frontal regions. An average increase in MiP
308 POC of about 25% is also observed for the first and the second features. Importantly, the three features occurred during the
309 surface production period and do not show a signature in smaller particle abundances (as indicated by the absence of such a

310 pattern in fluorescence and *bbsr*, Fig. 2.D-E). In particular, MiP and MaP abundances between 100 and 1000 m were

311 significantly correlated with intense FTLE values (Spearman's rank correlation coefficient of 0.4, p-value = 4.10^{-4} and 0.49,

312 p-value = $1.3.10^{-5}$ respectively, Fig. S3-S4). Mean MiP abundance, at this depth, was also significantly correlated with low

313 AOU values (coefficient correlation of -0.59, p-value = $1.6.10^{-8}$, Fig. S5).

314 **3 Discussion**

315 **3.1 Drivers of marine snow production in the surface layer**

316 The analysis of the chlorophyll-a time series helped to characterize the seasonality of primary production in our study area. In

317 particular, from the end of October 2021 to May 2022 (spanning spring and summer), there was a significant increase in surface

318 layer chlorophyll-a concentrations (Fig. 2.D). This observation is consistent with the existing knowledge on the seasonality of

319 phytoplankton in the southern part of the Atlantic Ocean (Thomalla et al., 2011) and led us to consider this period as the

320 productive period.

321 Regarding the spatiotemporal distribution of MiP and MaP (Fig. 3.B), the abundance of MaP (i.e. aggregates) in the surface

322 layer (0-100m) was significantly correlated with the surface Lagrangian chlorophyll and high FTLE, indicating a strong

323 biophysical coupling via several synergistic mechanisms (enhanced primary production, coagulation, transport). Ocean eddies,

324 especially cyclones, have the potential to enhance primary production by upwelling nutrient-rich water from deeper layers to

325 the surface (Cornec et al., 2021; Ascani et al., 2013; Benitez-Nelson et al., 2007). This leads to the biomass accumulation at

326 the edges of cyclones due to water mass divergence (water mass flow from the center to the cyclone periphery), resulting in

327 aggregate formation between submesoscale structures (Lima, 2002). Eddies can also move phytoplankton patches through

328 eddy stirring or trapping (McGillicuddy, 2016), leading to the accumulation of organic matter at the eddy boundaries (Fig.

329 10.1). This implies that actively growing phytoplankton transported by the water body in the previous days could have

330 contributed to increase the abundance of MaPs by aggregation of organic matter and biological activity. Among the MaP, large

331 particles classified as elongated type were mostly found at the surface and they were the best correlated with surface

332 chlorophyll-a. Their origin is difficult to assess, but their filamentous morphology makes them resemble chain-forming diatoms

333 or other phytoplankton colonies. The other categories of MaPs are also abundant and could be the result of the aggregation

334 into larger particles by biophysical coagulation or trophic activities. Coagulation is responsible for the production of large

335 particles when particle concentrations become important in the water column (Jackson et al.1990). Through this mechanism,

336 particle encounter rates are enhanced by Brownian motion, shear and/or differential settling resulting in the formation of a

337 single, larger particle (Jackson, 1990; Stemmann et al., 2004) on a timescale of a few days, as already suggested in the Southern

338 Ocean (Jouandet et al., 2014). By affecting photosynthesis and water movement, the observed intense mesoscale and

339 submesoscale dynamics, (Figs. 7-9), could significantly affect particle concentration and the probability of aggregation. The

340 second aggregation mechanism by zooplankton grazing, sloppy feeding (Lampitt et al., 1990) and fecal pellet production

341 (Turner, 2015), occurs at long temporal scales due to the slower growth time of zooplankton. Our observation strategy with a

342 float cannot rule this aggregation mechanism out. However, typical mesozooplankton fecal pellets (a few hundred µm) were
343 not observed in abundance in any of the four morphological categories. We haven't also observed a zooplankton abundance
344 increase during the three particle distribution events (see Figure S6). In our case, it is more likely that physical coagulation
345 had a greater influence on aggregate formation than trophic biological aggregation. In fact, MaP were present at the surface
346 only during the period of maximum chlorophyll-a concentration and were associated with intense FTLE values (greater than
347 0.45 days^{-1}), which can be used as a proxy of water masses convergence (i.e. frontal zones). In other words, they could benefit
348 from a combination of high hydrodynamic and strong phytoplankton production, consistent with the model analysis proposed
349 by Jackson (1990) for coagulation.

3.2 Coupling between massive export of large aggregates and regional ocean dynamics

351 Analysis of the spatio-temporal distribution of particles has revealed three regions of enhanced concentration of particles at
352 depth, suggesting that vertical export of organic matter occurred in these areas during the productive season. These were
353 characterized by intense MaP and MiP abundances extending vertically from the surface to depths of about 600 m. These
354 export regions were associated with high FTLE values suggesting frontogenesis-driven mechanisms during which there could
355 be a strong coupling between gravitational sinking of particles and intensified physical vertical velocities.

3.2.1 A submesoscale frontogenesis-driven mechanism

357 The abundance of particles such as MaP and MiP below the MLD (100-600m) was positively correlated with the surface
358 Lagrangian FTLE as well as for the small, bright and aggregated morphotypes. Large FTLE values can identify convergence
359 of water masses with different hydrological properties, creating intense density gradients. It is known that intense velocity and
360 density gradients arise in correspondence with mesoscale (geostrophic) and submesoscale (ageostrophic) frontogenesis, e.g. at
361 the edge of mesoscale features (Freilich and Mahadevan, 2021). At such fronts upper-ocean waters converge and subduct
362 beneath the mixed layer into the stratified pycnocline (e.g. Omand et al. 2015) or also in deeper layers (e.g. Llort et al., 2018).
363 These regions are typically associated with significant vertical velocities (up to 20 m/day). Frontal patterns, in the potential
364 density time series, are clearly seen extending into the ocean interior (Fig. 2.C) and are also found to correspond to the three
365 intense export features. During these features, the signal reached about 1000 m. All of them were located at the periphery of
366 mesoscale eddies (Figs. 7-9), where the vertical velocity is expected to be higher (Thomas et al., 2008; Freilich and Mahadevan,
367 2021). Unfortunately, it was not possible to calculate vertical velocities from the data provided by the BGC Argo profiler.

368 Previous studies in a similar mesoscale physical context have shown that mesoscale activity can result in the intrusion of small
369 POM-rich water masses into the mesopelagic layers (Omand et al., 2015; Llort et al., 2018). In our study, the three features
370 described, occurred from the MLD to a depth of about 600 m or deeper (i.e. over a large part of the water column), whereas
371 the subduction described in Llort et al. (2018) occurred well below the MLD in the mesopelagic in depth layers thickness of
372 about 50-100 m. This suggests that we are describing a slightly different mechanism compared to Omand et al. (2015) and

373 Llort et al. (2018) responsible for the accumulation of organic matter at depth, but also one related to mesoscale and
374 submesoscale processes. This highlights the fact that the influence of these physical mechanisms is a challenging area of
375 research.

3.2.2 The key role of the gravitational carbon pump and the MLD

377 Historically, particle size has been considered as the primary factor influencing settling velocity (Guidi et al., 2008). However,
378 with advances in imaging systems, it has become increasingly clear that particle morphology has a significant effect on settling
379 velocities (Iversen and Lampitt, 2020; Cael et al., 2021; Williams and Giering, 2022). This process supports the idea that larger
380 (large ESD, size characteristic) and more compact (non-porous, morphological property) particles will sink faster. In this study,
381 direct estimates of settling particle velocity (e.g. export plume methodology; Stemmann et al., 2002; Briggs et al., 2020;
382 Trudnowska et al., 2021) could not be computed due to the non-completely Lagrangian nature of the float. However, it is
383 possible to assume that the morphotypes identified in this work have different sinking velocities with the highest for
384 small/dense and dark aggregate morphotypes (which dominate in the deepest water column, Fig. 5.D) and the lowest for the
385 elongated morphotypes because they are only found at the surface (Fig. 5.B). In addition, the particles with the higher
386 velocities should be rapidly exported to depth, so they should spend less time in the upper water column than particles with
387 the lowest sinking velocity. In other words, the latter will be more exposed to remineralization.

388 Furthermore, the analysis of the morphotype distribution during the three export features showed a shift in the group
389 proportions between the surface layer (0-100m, which is approximately the mean depth of the MLD, all profiles included) and
390 deeper layers (100-1000m). This shift favored small and dense aggregate groups (in terms of proportion) between these two
391 layers. These morphotypes should have the highest sinking rate. This supports the idea that the MLD could act as a physical
392 barrier (Hosoda et al., 2010) and only sinking particles were able to cross it. This conclusion is also supported by the fact that,
393 in most profiles, only MiP and especially MaP are located below the MLD, while small labile and refractory particles (*bbsr*)
394 and chlorophyll-containing particles were rarely found below the MLD. Among the MaP, the sinking explanation is valid for
395 three morphotypes (small particles, bright and dense aggregates), but not for the elongated types that we hypothesized to be
396 large phytoplankton. This result further emphasizes the critical importance of considering morphology and not just particle
397 size when analyzing the size of particles in marine snow dynamics and when calculating vertical fluxes using only allometric
398 relationships.

399 Another result is that features 1 and 3 show minimal changes in morphotype proportions between layer depths. In fact, it would
400 be expected that the relative proportion of each morphotype would vary with depth due to their presumed different settling
401 rates. It is possible that the morphotypes do not have different settling rates and settle at similar rates. Alternatively, there may
402 be some other mechanism at work that is significantly more important than settling velocity and is responsible for transporting
403 particles to deeper regions, which will be discussed below.

3.2.3 Coupling with vertical velocities

During the three described features, MiP abundance between 100 and 1000 meters was significantly correlated with low AOU values. AOU is a proxy for the age of water masses (Sarmiento, 2006), with lower AOU values indicating that the water masses had a more recent contact with the surface. The significant negative correlation between AOU and 100-1000 m MiP abundance suggests a physical downward transport leading to the formation of these features. In addition, we know from the eddy detection algorithm that each export feature was detected in the frontal region separating two adjacent eddies of opposite polarity. Mesoscale activity is known to play an important role in the vertical distribution of water masses.

In addition, surface frontal regions develop ageostrophic secondary circulations (Lévy et al., 2018) that lead to intense vertical velocities, which can be stronger at the edges of cyclonic structures and can be on the order of 100 m d^{-1} or more (Capó et al., 2021; Freilich & Mahadevan, 2021; Tarry et al., 2021; Siegelman et al., 2020; Mahadevan et al., 2016; McWilliams, 2016; Mahadevan & Archer, 2000). This is further supported by several studies that show that the presence of mesoscale eddies greatly enhances the vertical transport of water properties (Omand et al., 2015, Llort et al., 2018, Couespel et al., 2024). In the study region, mesoscale ocean dynamics are particularly active, with eddies generated by the Agulhas Current (the Agulhas rings), the Agulhas Bank (the Agulhas lee cyclones), the Benguela upwelling, and subantarctic front cyclones. All can influence the water column to depths of up to 1600 meters (Schmid et al., 2003). While these dynamics are known to exist, their impact on the vertical exchange of properties through the water column remains to be assessed. However, a recent study (Siegelman et al., 2020) has shown that such vertical velocities are enhanced below the MLD, which acts as a buffer for them, by relatively deep submesoscale fronts. This result may explain why only large particles (i.e., MiP, MaP, and morphotypes) involved in the gravitational pump and capable of crossing the physical barrier represented by the MLD are entrained in this process. The hypothesis that the gravitational pump may be associated with physical processes related to mesoscale activity has already been proposed by Guidi et al. (2007). The authors found that the natural gravitational settling of particles combined with the associated vertical velocities of the water masses triggered the export of particles into the deep Atlantic. Such a physical mechanism associated with the gravitational pump would be a key process of carbon export to the deep ocean observed in our study.

4 Conclusion

As described in the conceptual schematic (Fig. 10), mesoscale frontal dynamics between cyclones and anticyclones seem to have a profound effect on particle distribution down to 600 m depth. We propose that particle concentration at these locations is enhanced by increased primary production and/or turbulence or trapping. As a result, coagulation processes may have been enhanced, with the ultimate result being the formation of larger aggregates. These particles could have sunk below the MLD, in particular the large and/or dense ones, due to their higher sinking velocities. The consistently observed vertical distribution of particles from the surface to a depth of 600 m suggests that their downward transport is extremely rapid. We propose that

435 such features result from a coupling between their own sedimentation rate (the gravitational carbon pump) and the enhanced
436 vertical motion of the water induced by submesoscale frontal dynamics, in particular below the MLD. If such a phenomenon
437 is influenced by deeper mesoscale structures, it is likely to extend into deeper layers. Such vertical transport is an integral part
438 of the physical particle injection pump, particularly a unique frontal subduction pump, characterized by intense vertical
439 velocities that might materialize in intense frontal regions.

440 Our study suggests that small-scale ocean dynamics represent an efficient particle injection pump that can enhance the
441 efficiency of the biological pump by increasing the depth of carbon transport. It is crucial to note that the explicit mechanisms
442 underlying these features are not fully defined due to the temporal and spatial limitations imposed by the Argo float's lack of
443 resolution. Additionally, the submesoscale nature of these features introduces high variability in both space and time. This
444 study underscores the significance of implementing repeated sampling campaigns or the use of gliders equipped with UVP6
445 and further sensors (e.g. microstructure) and focusing on the interface zones between eddies. Such studies would help to
446 validate our proposed mechanisms and would improve our understanding of the mechanisms involved in this process. Since
447 mesoscale and submesoscale structures are ubiquitous in the ocean, it would also be interesting to quantify the influence of
448 this type of process on the overall carbon budget and to determine the extent to which it contributes to carbon sequestration in
449 the deep ocean, information that is crucial in the context of global change.

450 **5 Author contribution**

451 A.A., R.K. and L.S.: designed the study
452 A.A.: conducted data analysis, interpreted results, drafted the manuscript, under guidance of RK and LS
453 AB and RL.: supported the study by environmental background data analysis, revised manuscript.
454 R.K. and S.S.: contributed to the conception of the study, revised manuscript.
455 R.K.: coordinated the recapture of the float
456 L.S.: contributed to the conception and design of the study, supervised the analysis, substantively revised the manuscript.

457 **6 Competing interests**

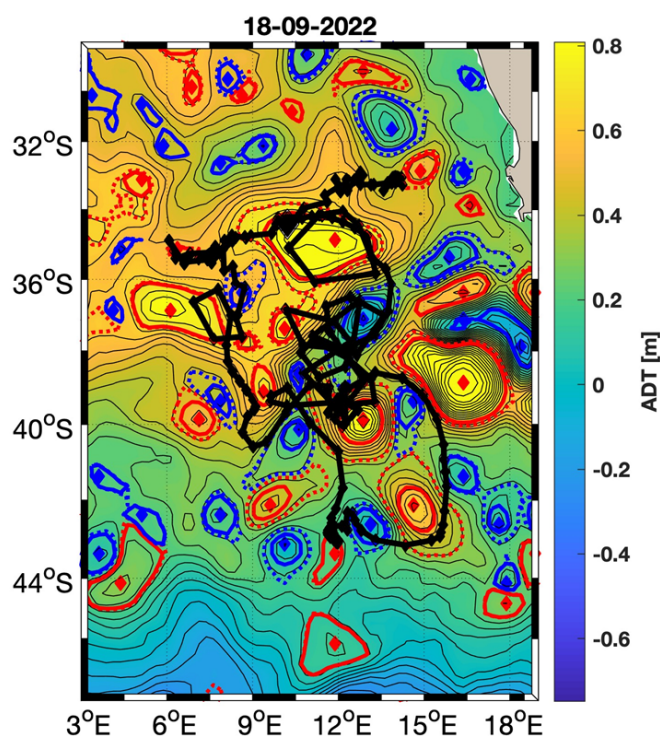458 The authors declare that they have no conflict of interest.

Figures

Figure 1: Float trajectory (thick black line) with profiles realized (185; black dots) during its deployment from April 2021 to September 2022. The map background is a snapshot of the ADT field in September 2022 showcasing the intense mesoscale activity of the study zone.

Figure 2: Hydrographic and biogeochemical properties as a function of time and depth along the float trajectory (1.5 years, from April 2021 to September 2022). The panels show (A) temperature, (B) salinity, (C) potential density, (D) chlorophyll-a concentration, (E) log10 of 700 nm optical backscatter bbsr, (F) Apparent Oxygen Utilization (AOU). The red solid line in each panel shows the mixed layer depth (MLD). The white dashed lines and the yellow stars show the location of intense exports of particles. The green triangles indicate the start and the end of the production period. Blue dots on top of the panel show the mean five days backward FTLE (days^{-1}) for each profile location.
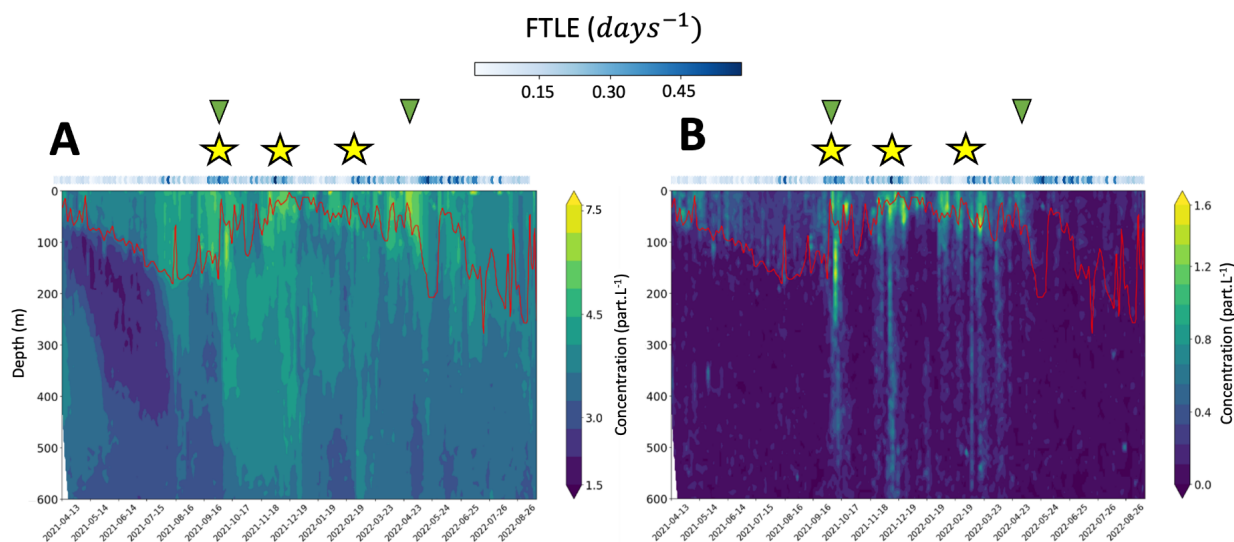
Figure 3: Particles spatio-temporal distribution. The panels show, (A) MiP (Micrometric Particles 0.1 < ESD < 0.5 mm) concentrations, (B) MaP (Macrometric Particles 0.6 < ESD < 16 mm) concentrations. Both concentrations were log transformed. Red solid line represents the MLD. Yellow stars show the location of intense exports of particles. Green triangles give the start and the end of the production period. Blue dots on top of the panels show five days backward FTLE (days⁻¹) for each profile location.
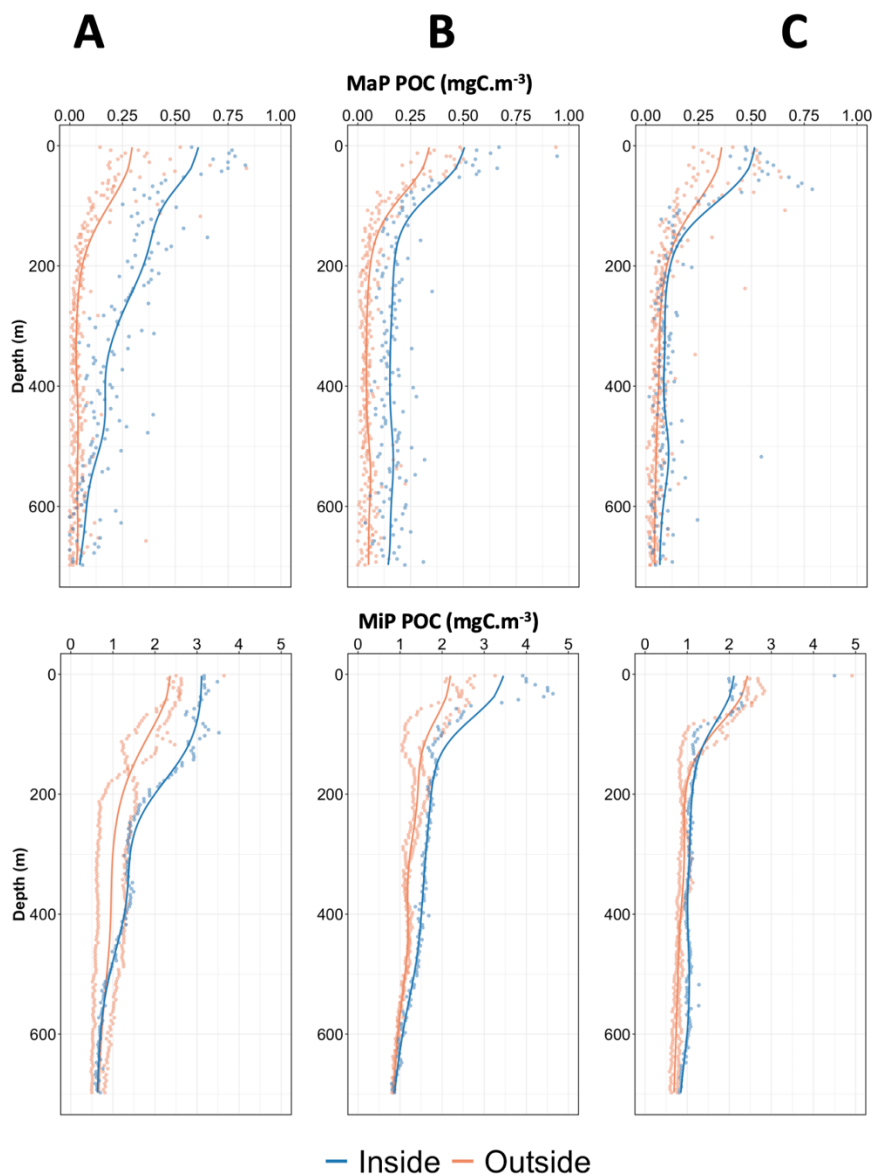
Figure 4: Comparison of MiP POC (top panels) and MaP POC (bottom panels) in the water column both outside and inside each export feature. The panels show, (A) the first export feature (01-10-2021 – 17/10/2021), (B) the second one (01-12-2021 – 19-12-2021) and (C) the last one (01/03/2022 – 28/03/2022). The dots on the graph represent the data averaged over 5-meter bins. The solid lines are a moving average of the 5-meter bins data. The orange signal corresponds to the average of profiles recorded one month prior to and after each feature (outside), while the blue signal corresponds to the average profiles recorded during each feature (inside).
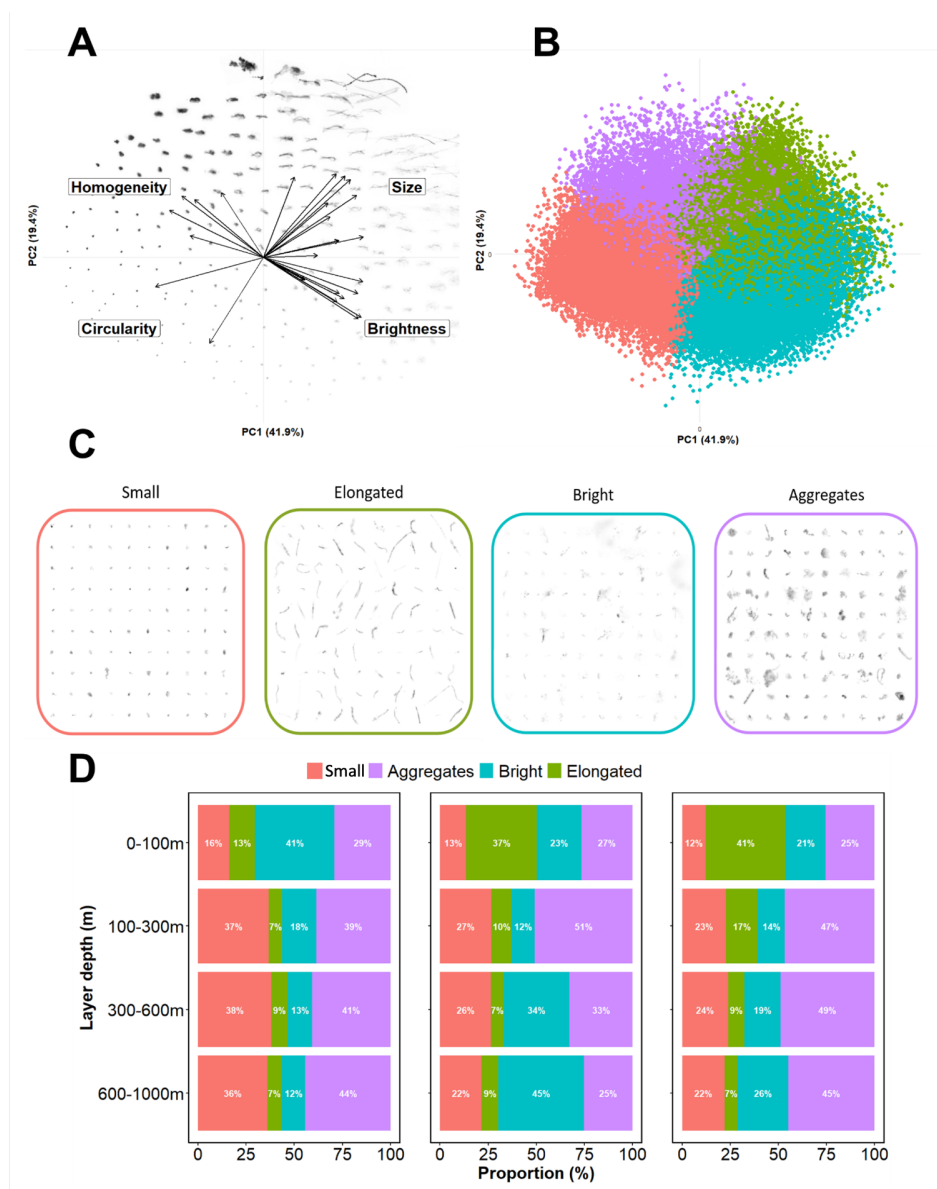
Figure 5: Results of PCA/K-means clustering on morphological traits of particles. Panels show, (A) the distribution of particle images in the morphospace built by PCA, (B) the K-means clustering classification where each point represents an image, and each cluster is colored independently. The yellow dots represent the center of each cluster. The most transparent dots represent images not retained in the analysis, (C) Representative subset of each morphotype and (D) the proportion (%) of each group according to depth layers during the three export features observed in the morphotypes spatio-temporal distribution. The color code is the same for (B), (C) and (D).
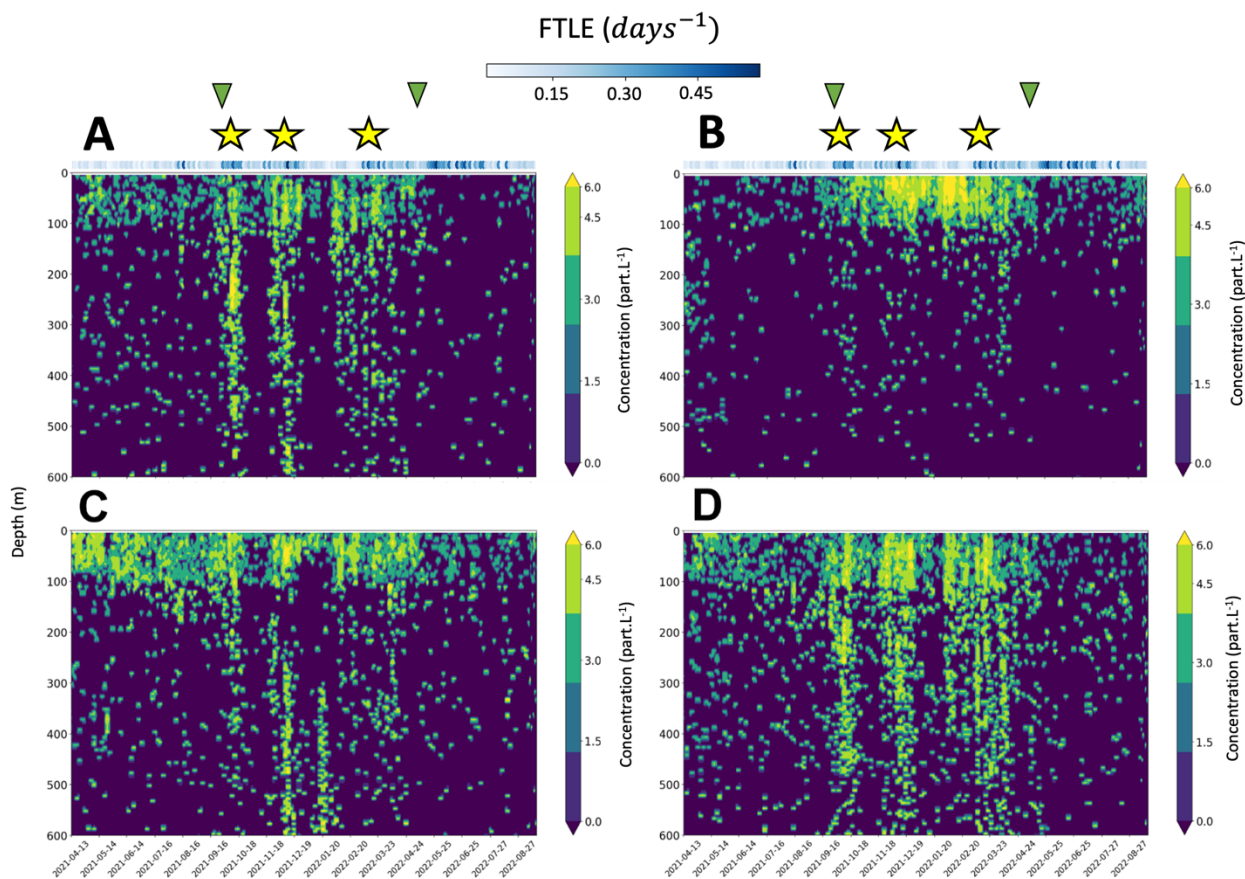
Figure 6: Morphotypes spatio-temporal distribution of exclusive members. The panels show log transformed concentrations (*part.L⁻¹*) of (A) Small, (B) Elongated, (C) Bright and (D) Aggregates morphotypes. White dashed lines, yellow stars and green triangles have the same meaning as in the Figure 2
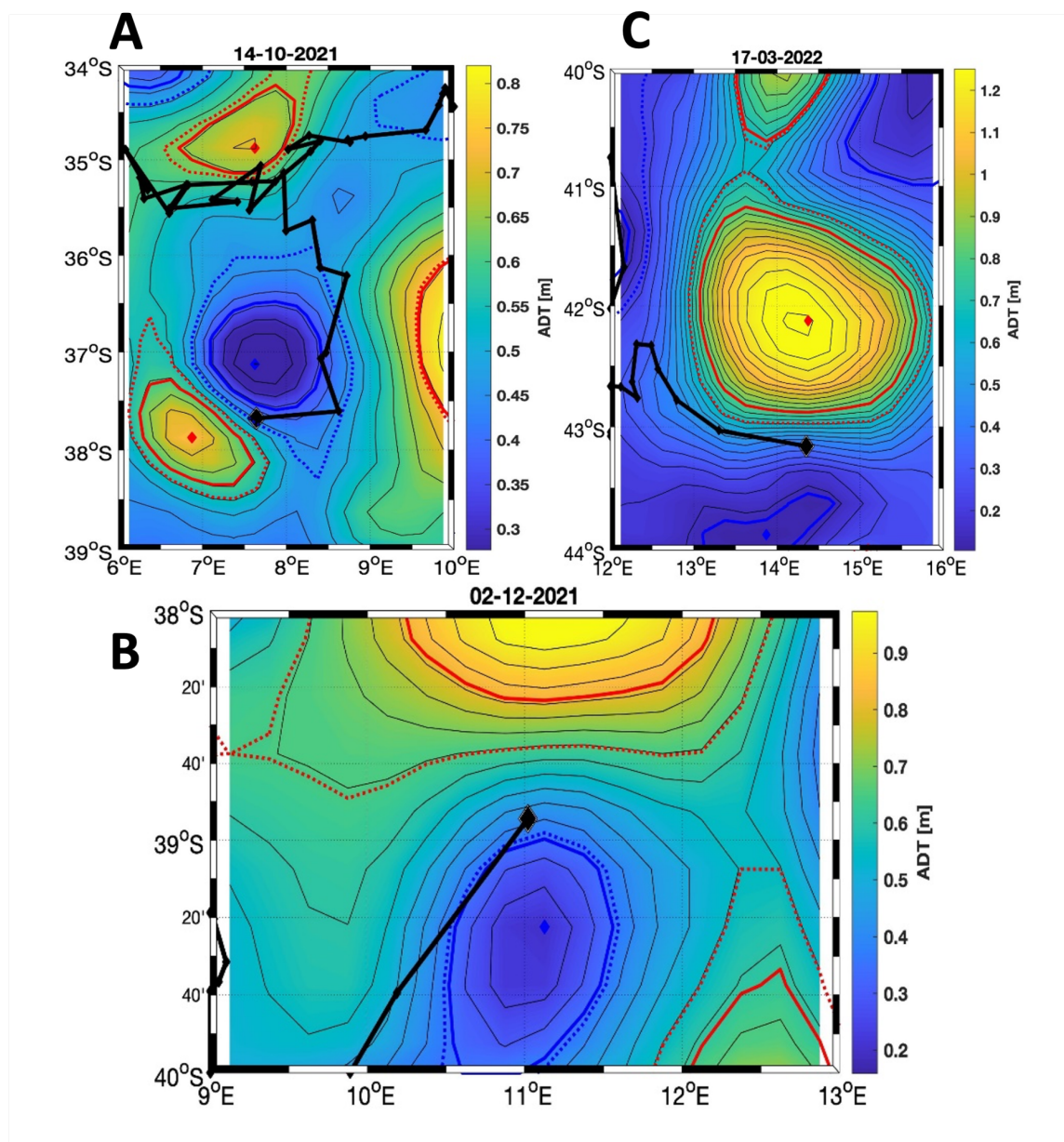
Figure 7: Snapshot of ADT field with the float trajectory (thick black line) during each export feature (A, B and C). Cyclones and anticyclones are associated with blue and red colors, respectively. Diamonds show eddy centroids. Solid lines correspond to the eddy maximum speed. Dashed line to the eddy outer limit definition.
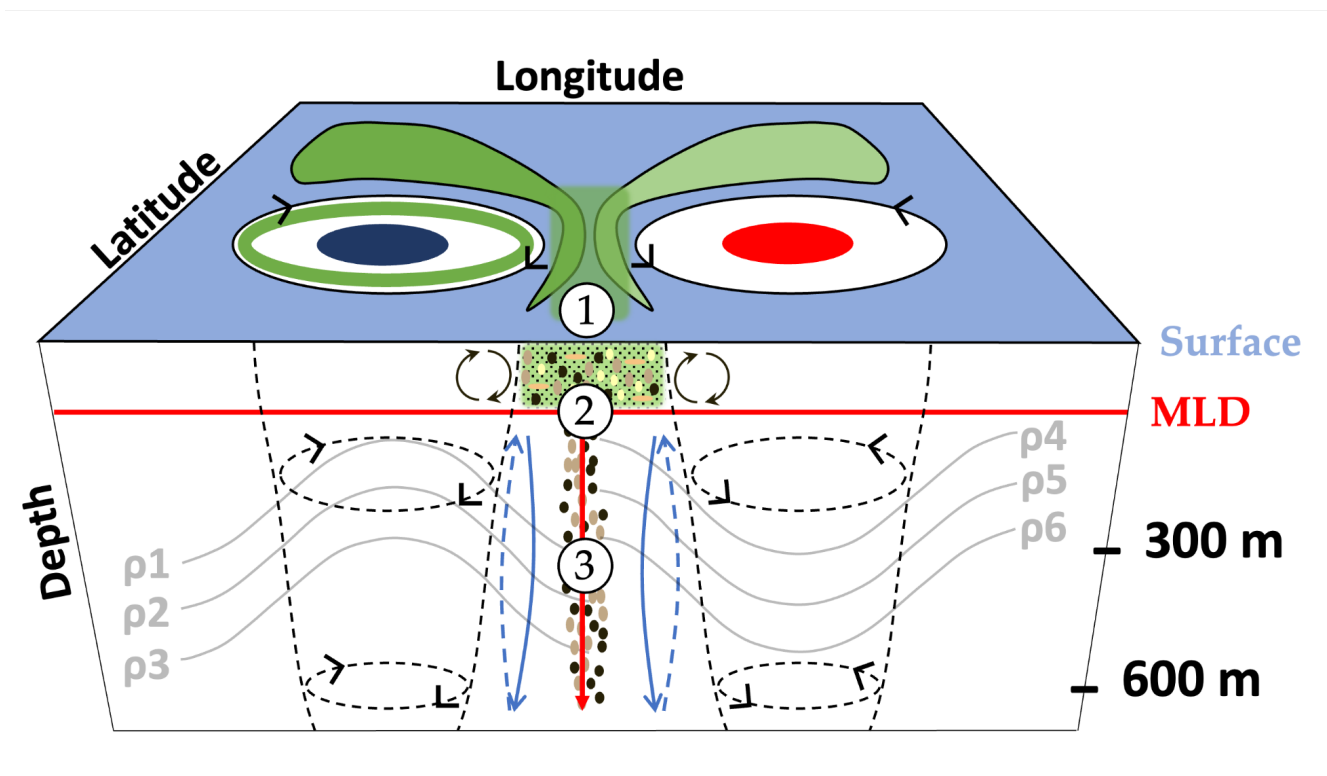
Figure 8: Schematic view of the proposed mechanism for the deep observed accumulation of particulate carbon in the mesoscale context of the study. (1) Aggregation and coagulation of surface organic matter, facilitated by eddy trapping or stirring. (2) Influence of the Gravitational Carbon Pump (represented by the red vertical arrow) that transporting particles with sufficient downward speed beneath the Mixed Layer Depth (MLD). (3) Coupling with a frontogenesis mechanism inducing enhanced physical vertical speeds (represented by blue arrows), particularly below the MLD and in interface zones between mesoscale structures. The coupling between (1), (2) and (3) can lead to the transport of particles down to significant depths (600 meters in our study). Black arrows in the MLD represent the physical mixing.

References

Alldredge, A. L. and Gotschalk, C.: In situ settling behavior of marine snow1: Sinking rates of marine snow, Limnol. Oceanogr., 33, 339–351, https://doi.org/10.4319/lo.1988.33.3.0339, 1988.

Ascani, F., Richards, K. J., Firing, E., Grant, S., Johnson, K. S., Jia, Y., Lukas, R., and Karl, D. M.: Physical and biological controls of nitrate concentrations in the upper subtropical North Pacific Ocean, Deep Sea Research Part II: Topical Studies in Oceanography, 93, 119–134, https://doi.org/10.1016/j.dsr2.2013.01.034, 2013.

Azetsu-Scott, K. and Johnson, B. D.: Measuring physical characteristics of particles: a new method of simultaneous measurement for size, settling velocity and density of constituent matter, Deep Sea Research Part A. Oceanographic Research Papers, 39, 1057–1066, https://doi.org/10.1016/0198-0149(92)90039-V, 1992.

Ballarotta, M., Ubelmann, C., Pujol, M.-I., Taburet, G., Fournier, F., Legeais, J.-F., Faugère, Y., Delepoulle, A., Chelton, D., Dibarboure, G., and Picot, N.: On the resolutions of ocean altimetry maps, Ocean Sci., 15, 1091–1109, https://doi.org/10.5194/os-15-1091-2019, 2019.

Barabinot, Y., Speich, S., and Carton, X. J.: Defining Mesoscale Eddies Boundaries from In-situ Data and a Theoretical Framework, Preprints, https://doi.org/10.22541/essoar.167870447.76933252/v1, 2023.

Baudena, A., Ser-Giacomi, E., D'Onofrio, D., Capet, X., Cotté, C., Cherel, Y., and D'Ovidio, F.: Fine-scale structures as spots of increased fish concentration in the open ocean, Sci Rep, 11, 15805, https://doi.org/10.1038/s41598-021-94368-1, 2021.

Baudena, A., Laxenaire, R., Catalano, C., Claustre, H., Ioannou, A., Leymarie, E., Picheral, M., Poteau, A., Speich, S., Stemmann, L., and Kiko, R.: A Lagrangian perspective on the carbon and oxygen budget of an oceanic eddy, preprint, https://doi.org/10.21203/rs.3.rs-3014931/v1, 2023.

Benitez-Nelson, C. R., Bidigare, R. R., Dickey, T. D., Landry, M. R., Leonard, C. L., Brown, S. L., Nencioli, F., Rii, Y. M., Maiti, K., Becker, J. W., Bibby, T. S., Black, W., Cai, W.-J., Carlson, C. A., Chen, F., Kuwahara, V. S., Mahaffey, C., McAndrew, P. M., Quay, P. D., Rappé, M. S., Selph, K. E., Simmons, M. P., and Yang, E. J.: Mesoscale Eddies Drive Increased Silica Export in the Subtropical Pacific Ocean, Science, 316, 1017–1021, https://doi.org/10.1126/science.1136221, 2007.

Benson, B. B. and Krause, D.: The concentration and isotopic fractionation of oxygen dissolved in freshwater and seawater in equilibrium with the atmosphere1: Oxygen solubility in seawater, Limnol. Oceanogr., 29, 620–632, https://doi.org/10.4319/lo.1984.29.3.0620, 1984.

Boyd, P. W., Claustre, H., Levy, M., Siegel, D. A., and Weber, T.: Multi-faceted particle pumps drive carbon sequestration in the ocean, Nature, 568, 327–335, https://doi.org/10.1038/s41586-019-1098-2, 2019.

Briggs, N., Dall'Olmo, G., and Claustre, H.: Major role of particle fragmentation in regulating biological sequestration of CO_2 by the oceans, Science, 367, 791–793, https://doi.org/10.1126/science.aay1790, 2020.

729   Cael, B. B., Cavan, E. L., and Britten, G. L.: Reconciling the Size-Dependence of Marine Particle Sinking Speed, Geophysical
730   Research Letters, 48, https://doi.org/10.1029/2020GL091771, 2021.

731   Capó, E., McWilliams, J. C., Mason, E., and Orfila, A.: Intermittent Frontogenesis in the Alboran Sea, Journal of Physical
732   Oceanography, 51, 1417–1439, https://doi.org/10.1175/JPO-D-20-0277.1, 2021.

733   Chaigneau, A., Eldin, G., and Dewitte, B.: Eddy activity in the four major upwelling systems from satellite altimetry (1992–
734   2007), Progress in Oceanography, 83, 117–123, https://doi.org/10.1016/j.pocean.2009.07.012, 2009.

735   Chambault, P., Baudena, A., Bjorndal, K. A., Santos, M. A. R., Bolten, A. B., and Vandeperre, F.: Swirling in the ocean:
736   Immature loggerhead turtles seasonally target old anticyclonic eddies at the fringe of the North Atlantic gyre, Progress in
737   Oceanography, 175, 345–358, https://doi.org/10.1016/j.pocean.2019.05.005, 2019.

738   Cornec, M., Laxenaire, R., Speich, S., and Claustre, H.: Impact of Mesoscale Eddies on Deep Chlorophyll Maxima,
739   Geophysical Research Letters, 48, e2021GL093470, https://doi.org/10.1029/2021GL093470, 2021.

740   Couespel, D., Lévy, M., and Bopp, L.: Stronger oceanic CO_2 sink in eddy-resolving simulations of global warming,
741   Geophysical Research Letters, https://hal.science/hal-04396517/, 2024.

742   De Boyer Montégut, C., Madec, G., Fischer, A. S., Lazar, A., and Iudicone, D.: Mixed layer depth over the global ocean: An
743   examination of profile data and a profile-based climatology, J. Geophys. Res., 109, 2004JC002378,
744   https://doi.org/10.1029/2004JC002378, 2004.

745   Duncombe Rae, C. M.: Agulhas retroflection rings in the South Atlantic Ocean: an overview, South African Journal of Marine
746   Science, 11, 327–344, https://doi.org/10.2989/025776191784287574, 1991.

747   Fabri-Ruiz, S., Baudena, A., Moullec, F., Lombard, F., Irisson, J.-O., and Pedrotti, M. L.: Mistaking plastic for zooplankton:
748   Risk assessment of plastic ingestion in the Mediterranean sea, Science of The Total Environment, 856, 159011,
749   https://doi.org/10.1016/j.scitotenv.2022.159011, 2023.

750   Freilich, M. A. and Mahadevan, A.: Decomposition of Vertical Velocity for Nutrient Transport in the Upper Ocean, Journal
751   of Physical Oceanography, 49, 1561–1575, https://doi.org/10.1175/JPO-D-19-0002.1, 2019.

752   Garcia, H. E. and Gordon, L. I.: Oxygen solubility in seawater: Better fitting equations, Limnol. Oceanogr., 37, 1307–1312,
753   https://doi.org/10.4319/lo.1992.37.6.1307, 1992.

754   Guidi, L., Stemmann, L., Legendre, L., Picheral, M., Prieur, L., and Gorsky, G.: Vertical distribution of aggregates (>110 µm)
755   and mesoscale activity in the northeastern Atlantic: Effects on the deep vertical export of surface carbon, Limnol. Oceanogr.,
756   52, 7–18, https://doi.org/10.4319/lo.2007.52.1.0007, 2007.

757 Guidi, L., Jackson, G. A., Stemmann, L., Miquel, J. C., Picheral, M., and Gorsky, G.: Relationship between particle size
758 distribution and flux in the mesopelagic zone, Deep Sea Research Part I: Oceanographic Research Papers, 55, 1364–1374,
759 https://doi.org/10.1016/j.dsr.2008.05.014, 2008.

760 Hosoda, S., Ohira, T., Sato, K., and Suga, T.: Improved description of global mixed-layer depth using Argo profiling floats, J
761 Oceanogr, 66, 773–787, https://doi.org/10.1007/s10872-010-0063-3, 2010.

762 Ioannou, A., Speich, S., and Laxenaire, R.: Characterizing Mesoscale Eddies of Eastern Upwelling Origins in the Atlantic
763 Ocean and Their Role in Offshore Transport, Front. Mar. Sci., 9, 835260, https://doi.org/10.3389/fmars.2022.835260, 2022.

764 Iversen, M. H. and Lampitt, R. S.: Size does not matter after all: No evidence for a size-sinking relationship for marine snow,
765 Progress in Oceanography, 189, 102445, https://doi.org/10.1016/j.pocean.2020.102445, 2020.

766 Jackson, G. A.: A model of the formation of marine algal flocs by physical coagulation processes, Deep Sea Research Part A.
767 Oceanographic Research Papers, 37, 1197–1211, https://doi.org/10.1016/0198-0149(90)90038-W, 1990.

768 Lampitt, R. S., Noji, T., and Von Bodungen, B.: What happens to zooplankton faecal pellets? Implications for material flux,
769 Mar. Biol., 104, 15–23, https://doi.org/10.1007/BF01313152, 1990.

770 Laxenaire, R., Speich, S., Blanke, B., Chaigneau, A., Pegliasco, C., and Stegner, A.: Anticyclonic Eddies Connecting the
771 Western Boundaries of Indian and Atlantic Oceans, J. Geophys. Res. Oceans, 123, 7651–7677,
772 https://doi.org/10.1029/2018JC014270, 2018.

773 Laxenaire, R., Speich, S., and Stegner, A.: Evolution of the Thermohaline Structure of One Agulhas Ring Reconstructed from
774 Satellite Altimetry and Argo Floats, J. Geophys. Res. Oceans, 124, 8969–9003, https://doi.org/10.1029/2018JC014426, 2019.

775 Laxenaire, R., Speich, S., and Stegner, A.: Agulhas Ring Heat Content and Transport in the South Atlantic Estimated by
776 Combining Satellite Altimetry and Argo Profiling Floats Data, JGR Oceans, 125, e2019JC015511,
777 https://doi.org/10.1029/2019JC015511, 2020.

778 Le Moigne, F. A. C.: Pathways of Organic Carbon Downward Transport by the Oceanic Biological Carbon Pump, Front. Mar.
779 Sci., 6, 634, https://doi.org/10.3389/fmars.2019.00634, 2019.

780 Lévy, M., Franks, P. J. S., and Smith, K. S.: The role of submesoscale currents in structuring marine ecosystems, Nat Commun,
781 9, 4758, https://doi.org/10.1038/s41467-018-07059-3, 2018.

782 Lima, I. D.: Biological response to frontal dynamics and mesoscale variability in oligotrophic environments: Biological
783 production and community structure, J. Geophys. Res., 107, 3111, https://doi.org/10.1029/2000JC000393, 2002.

784 Llort, J., Langlais, C., Matear, R., Moreau, S., Lenton, A., and Strutton, P. G.: Evaluating Southern Ocean Carbon Eddy-Pump
785 From Biogeochemical-Argo Floats, JGR Oceans, 123, 971–984, https://doi.org/10.1002/2017JC012861, 2018.

786   Lutjeharms, J. R. E., Boebel, O., and Rossby, H. T.: Agulhas cyclones, Deep Sea Research Part II: Topical Studies in
787   Oceanography, 50, 13–34, https://doi.org/10.1016/S0967-0645(02)00378-8, 2003.

788   Mahadevan, A.: The Impact of Submesoscale Physics on Primary Productivity of Plankton, Annu. Rev. Mar. Sci., 8, 161–184,
789   https://doi.org/10.1146/annurev-marine-010814-015912, 2016.

790   Mahadevan, A. and Archer, D.: Modeling the impact of fronts and mesoscale circulation on the nutrient supply and
791   biogeochemistry of the upper ocean, J. Geophys. Res., 105, 1209–1225, https://doi.org/10.1029/1999JC900216, 2000.

792   McGillicuddy, D. J.: Mechanisms of Physical-Biological-Biogeochemical Interaction at the Oceanic Mesoscale, Annu. Rev.
793   Mar. Sci., 8, 125–159, https://doi.org/10.1146/annurev-marine-010814-015606, 2016.

794   McWilliams, J. C.: Submesoscale currents in the ocean, Proc. R. Soc. A., 472, 20160117,
795   https://doi.org/10.1098/rspa.2016.0117, 2016.

796   Omand, M. M., D'Asaro, E. A., Lee, C. M., Perry, M. J., Briggs, N., Cetinić, I., and Mahadevan, A.: Eddy-driven subduction
797   exports particulate organic carbon from the spring bloom, Science, 348, 222–225, https://doi.org/10.1126/science.1260062,
798   2015.

799   Penven, P., Lutjeharms, J. R. E., Marchesiello, P., Roy, C., and Weeks, S. J.: Generation of cyclonic eddies by the Agulhas
800   Current in the Lee of the Agulhas Bank, Geophys. Res. Lett., 28, 1055–1058, https://doi.org/10.1029/2000GL011760, 2001.

801   Picheral, M., Catalano, C., Brousseau, D., Claustre, H., Coppola, L., Leymarie, E., Coindat, J., Dias, F., Fevre, S., Guidi, L.,
802   Irisson, J. O., Legendre, L., Lombard, F., Mortier, L., Penkerch, C., Rogge, A., Schmechtig, C., Thibault, S., Tixier, T., Waite,
803   A., and Stemmann, L.: THE UNDERWATER VISION PROFILER 6: AN IMAGING SENSOR OF PARTICLE SIZE SPECTRA AND PLANKTON,
804   FOR AUTONOMOUS AND CABLED PLATFORMS, Limnology & Ocean Methods, 20, 115–129, https://doi.org/10.1002/lom3.10475,
805   2022.

806   Pujol, M.-I., Faugère, Y., Taburet, G., Dupuy, S., Pelloquin, C., Ablain, M., and Picot, N.: DUACS DT2014: the new multi-
807   mission altimeter data set reprocessed over 20 years, Ocean Sci., 12, 1067–1090, https://doi.org/10.5194/os-12-1067-2016,
808   2016.

809   Richardson, P. L., Lutjeharms, J. R. E., and Boebel, O.: Introduction to the "Inter-ocean exchange around southern Africa,"
810   Deep Sea Research Part II: Topical Studies in Oceanography, 50, 1–12, https://doi.org/10.1016/S0967-0645(02)00376-4,
811   2003.

812   Rodionov, S. N.: A sequential algorithm for testing climate regime shifts: ALGORITHM FOR TESTING REGIME SHIFTS,
813   Geophys. Res. Lett., 31, n/a-n/a, https://doi.org/10.1029/2004GL019448, 2004.

814   Roquet, F., Madec, G., McDougall, T. J., and Barker, P. M.: Accurate polynomial expressions for the density and specific
815   volume of seawater using the TEOS-10 standard, Ocean Modelling, 90, 29–43, https://doi.org/10.1016/j.ocemod.2015.04.002,
816   2015.

817   Sarmiento, J. L.: Ocean Biogeochemical Dynamics, Princeton University Press, https://doi.org/10.1515/9781400849079,
818   2006.

819   Schmid, C., Boebel, O., Zenk, W., Lutjeharms, J. R. E., Garzoli, S. L., Richardson, P. L., and Barron, C.: Early evolution of
820   an Agulhas Ring, Deep Sea Research Part II: Topical Studies in Oceanography, 50, 141–166, https://doi.org/10.1016/S0967-
821   0645(02)00382-X, 2003.

822   Ser-Giacomi, E., Baudena, A., Rossi, V., Follows, M., Clayton, S., Vasile, R., López, C., and Hernández-García, E.:
823   Lagrangian betweenness as a measure of bottlenecks in dynamical systems with oceanographic examples, Nat Commun, 12,
824   4935, https://doi.org/10.1038/s41467-021-25155-9, 2021.

825   Shadden, S. C., Lekien, F., and Marsden, J. E.: Definition and properties of Lagrangian coherent structures from finite-time
826   Lyapunov exponents in two-dimensional aperiodic flows, Physica D: Nonlinear Phenomena, 212, 271–304,
827   https://doi.org/10.1016/j.physd.2005.10.007, 2005.

828   Shanks, A. L. and Trent, J. D.: Marine snow: sinking rates and potential role in vertical flux, Deep Sea Research Part A.
829   Oceanographic Research Papers, 27, 137–143, https://doi.org/10.1016/0198-0149(80)90092-8, 1980.

830   Siegelman, L., Klein, P., Rivière, P., Thompson, A. F., Torres, H. S., Flexas, M., and Menemenlis, D.: Enhanced upward heat
831   transport at deep submesoscale ocean fronts, Nat. Geosci., 13, 50–55, https://doi.org/10.1038/s41561-019-0489-1, 2020.

832   Stammer, D.: Global Characteristics of Ocean Variability Estimated from Regional TOPEX/POSEIDON Altimeter
833   Measurements, J. Phys. Oceanogr., 27, 1743–1769, https://doi.org/10.1175/1520-0485(1997)027<1743:GCOOVE>2.0.CO;2,
834   1997.

835   Stemmann, L., Jackson, G. A., and Ianson, D.: A vertical model of particle size distributions and fluxes in the midwater column
836   that includes biological and physical processes—Part I: model formulation, Deep Sea Research Part I: Oceanographic Research
837   Papers, 51, 865–884, https://doi.org/10.1016/j.dsr.2004.03.001, 2004.

838   Tarry, D. R., Essink, S., Pascual, A., Ruiz, S., Poulain, P., Özgökmen, T., Centurioni, L. R., Farrar, J. T., Shcherbina, A.,
839   Mahadevan, A., and D'Asaro, E.: Frontal Convergence and Vertical Velocity Measured by Drifters in the Alboran Sea, J.
840   Geophys. Res. Oceans, 126, https://doi.org/10.1029/2020JC016614, 2021.

841   Thomas, L. N., Tandon, A., and Mahadevan, A.: Submesoscale processes and dynamics, in: Geophysical Monograph Series,
842   vol. 177, edited by: Hecht, M. W. and Hasumi, H., American Geophysical Union, Washington, D. C., 17–38,
843   https://doi.org/10.1029/177GM04, 2008.

844 Trudnowska, E., Lacour, L., Ardyna, M., Rogge, A., Irisson, J. O., Waite, A. M., Babin, M., and Stemmann, L.: Marine snow
845 morphology illuminates the evolution of phytoplankton blooms and determines their subsequent vertical export, Nat Commun,
846 12, 2816, https://doi.org/10.1038/s41467-021-22994-4, 2021.

847 Turner, J. T.: Zooplankton fecal pellets, marine snow, phytodetritus and the ocean's biological pump, Progress in
848 Oceanography, 130, 205–248, https://doi.org/10.1016/j.pocean.2014.08.005, 2015.

849 Wunsch, C.: Where do ocean eddy heat fluxes matter?, J. Geophys. Res., 104, 13235–13249,
850 https://doi.org/10.1029/1999JC900062, 1999.

851 Yeo, I.-K.: A new family of power transformations to improve normality or symmetry, Biometrika, 87, 954–959,
852 https://doi.org/10.1093/biomet/87.4.954, 2000.

853